RADAR IMAGING MECHANISM OF MARINE SAND WAVES
AT VERY LOW GRAZING ANGLE ILLUMINATION

Ingo Hennings and Dagmar Herbers

Leibniz-Institut für Meereswissenschaften an der Universität Kiel (IFM-GEOMAR),
24148 Kiel, Germany; ihennings(at)ifm-geomar.de

ABSTRACT

The investigations carried out between 2002-2004 during several field experiments within the *Operational radar and optical mapping in monitoring hydrodynamic, morphodynamic and environmental parameters for coastal management project* (OROMA) aimed to improve the effectiveness of new monitoring technologies such as shipborne imaging radars in coastal waters. The coastal monitoring radar of the GKSS Research Centre, Geesthacht, Germany, is based on a Kelvin Hughes RSR 1000 X-band (9.42 GHz) VV polarized river radar and was mounted on board the research vessel *Ludwig Prandtl* during the experiments in the Lister Tief, a tidal inlet of the German Bight in the North Sea. The important progress realized in this investigation is the availability of calibrated X-band radar data. Another central point of the study is to demonstrate the applicability of the quasi-specular scattering theory in combination with the weak hydrodynamic interaction theory for the radar imaging mechanism of the sea bed. It is shown that specular point scattering contributes significantly to the normalized radar cross section (NRCS) modulation due to marine sand waves. According to the theory quasi-specular scattering can be applied for wind speeds $U_w \leq 8$ m s^{-1}. Measured and simulated NRCS modulations caused by flood and ebb tide oriented marine sand waves have been compared and agree fairly well.

Keywords: Marine sand waves, normalized radar cross section (NRCS) modulation, quasi-specular scattering theory, weak hydrodynamic interaction theory.

INTRODUCTION

Signatures of normalized radar cross section (NRCS) modulation at the ocean surface due to sea bottom topography are visible on a variety of radar images acquired by shore- and ship-based radar as well as by Real Aperture Radar (RAR) and Synthetic Aperture Radar (SAR) on board air- and spaceborne platforms (1,2,3,4). A first descriptive explanation of such phenomena was given by (5) and co-workers in the Netherlands. They had noticed surface manifestations of marine sand waves in coastal waters in K_a-band airborne radar imagery acquired on 19 September 1969, one hour before low tide on the Dutch coast of the southern North Sea. SEASAT, the first satellite specifically designed to study the oceans, was launched in 1978. The SEASAT L-band SAR recorded spectacular images of bottom topography in coastal seas < 50 m water depth like the Great Bahama Bank Southern Edge Tongue of the Ocean, the southern North Sea, the English Channel, the Thames Estuary, the Irish Sea, the Bristol Channel, and the Nantucket Shoals (6,7). These bathymetric features stimulated many research activities because the radar imaging mechanism of such phenomena was not well understood at that time. Theoretical models of the radar imaging mechanism of sea bottom topography have been described and discussed by (6,7,8,9,10,11,12).

An overview of general spatial scales of bed-forms and ocean floor topography as a function of water depth using different remote sensing radar systems has been presented by (13). Imaging radars are used for the detection of tidal current ridges, sand waves, and other morphological changes of the sea floor in water depths ≤ 50 m. The private company ARGOSS, in the Netherlands, has improved their depth monitoring system based on the two-dimensional version of the Bathymetry Assessment System (BAS-2D) for mapping water depths of shallow coastal waters using SAR and echo sounding data only (14,15). A technique of rewriting classical physical models as a series of nonlinear filters using Volterra models has been presented by (16). Applying this

technique the inversion algorithm avoids the use of an iterative data assimilation scheme. Their method is based only on the physical knowledge of the imaging mechanism which is expressed by the so-called Volterra kernels. The aim of this paper is to investigate if the quasi-specular scattering theory can be applied at very low grazing angle illumination to explain the X-band radar imaging mechanism of marine sand waves caused by unique hydrodynamic interactions.

The quasi-specular scattering theory is described in the second section and all methods applied in the study area of the Lister Tief in the German Bight of the North Sea are presented in the third section. In the fourth section the sea bed morphology associated with mesoscale dynamics and simulated, as well as measured NRCS modulation data, respectively, are described in subsections. Finally, the last section contains the discussion and conclusions.

THEORY

For most ocean wave conditions and radar incidence angles greater than 15°, the quasi-specular point scattering contribution to the mean radar image intensity is small compared with the Bragg scattering contribution. Under some local conditions there are indications that it may also contribute at larger incidence angles than 15°. It is well known that the magnitudes of water surface slopes, the directional character of the sea surface roughness and the level of microwave scattering are related in complicated ways to wind, fetch, current gradients, atmosphere stability, and other meteorological and oceanographic parameters. The nature of these dependencies and interactions are active and controversial areas of research. Specular reflection occurs when radiation is scattered into a given direction from surface regions with slopes such that the local specular direction coincides with the scattering direction. The quasi-specular scattering theory can be applied if the wavelengths of ocean waves contributing to the mean square surface slope are greater than the wavelength of the microwave. In general, the mean squared slope of ocean waves is small. This is considerably different, however, if waves are influenced by a surface current gradient. Very steep disturbed slopes of the order of 10° can arise in the converging zone of the current correlated with the slope regions of marine sand waves. Especially trochoidal shapes of water waves can be generated due to such a wave-current interaction at low to moderate wind speeds. These trochoidal shaping waves produce an ensemble average of facets which create quasi perpendicular planes relative to the transmitted radar beam. This could be an indication that short water waves contribute more as specular scattering targets to the imaging mechanism than predicted from the probability density function of slopes of the rough ocean surface without existing wave-current interaction. There exist also steep small gravity waves in this zone which tend to become sharp wedges just before they break and breaking waves themselves. In this paper we investigate if the quasi-specular scattering theory in combination with the weak hydrodynamic interaction theory can be applied to extremely steep slopes acting as backscattered mirrors.

The normalized radar backscattering cross section (NRCS) σ_o for an isotropic rough ocean surface obeying Gaussian statistics according to the incident angle dependency for quasi-specular scattering is given by (17):

$$\sigma_o(\theta_o) = \frac{|R(0)|^2}{s_o^2} \frac{1}{\cos^4 \theta_o} \exp\left(-\frac{\tan^2 \theta_o}{s_o^2}\right) \qquad (1)$$

where $R(0)$ is the Fresnel reflection coefficient for normal incidence, θ_o is the angle of incidence, and s_o^2 is the total variance of slopes created by ocean waves.

For the total variance of slopes the mean square slope of water waves derived by (18) empirically is used:

$$s_o^2 = 0.003 + 0.00512\, U_w \pm 0.004 \qquad (2)$$

where U_w is the wind speed.

Rewriting the total variance of slopes and the incidence angle as sums of a constant equilibrium term and a time-dependent perturbation term, respectively, yields

$$s^2 = s_o^2 + \delta s^2 \tag{3}$$

and
$$\theta = \theta_0 + \delta\theta \tag{4}$$

In the following the effective incidence angle θ_o is used for a real sea surface with roughness which no longer coincides with the incidence angle for a plane sea surface. The effective incidence angle θ_o is then given by:

$$\theta_o = \theta_{plane} + \theta_{rough} \tag{5}$$

where θ_{plane} is the incidence angle for a plane surface. The incidence direction of radar transmission is placed in a plane which is defined perpendicularly to the air-water boundary plane and hence includes also the normal relative to this boundary plane. The incidence angle is thereupon defined between this normal and the incident ray transmitted from the radar antenna. Here the incidence angle θ_{plane} is identical to the complementary angle called grazing angle (Figure 3).

The square tangent of the incidence angle of the background rough sea surface as a function of U_w (see Eq. (2)) is derived by:

$$\tan^2\theta_{rough} = s_o^2 \tag{6}$$

As a first approximation assuming that the time-dependent perturbation terms in Eqs. (3)-(4) caused by the disturbance of the surface current $\delta U(\vec{x})$ due to marine sand waves obey also Gaussian distributions, then the disturbed NRCS $\delta\sigma$ is given by:

$$\delta\sigma = \sigma - \sigma_0 = \frac{|R(0)|^2}{(s_o^2 + \delta s^2)\cos^4(\theta_o + \delta\theta)} \exp\left(-\frac{\tan^2(\theta_o + \delta\theta)}{s_o^2 + \delta s^2}\right) - \sigma_0 \tag{7}$$

where σ is the local NRCS. The NRCS modulation $\delta\sigma/\sigma_o$ due to quasi-specular scattering is defined by:

$$\frac{\delta\sigma}{\sigma_0} = \frac{\sigma}{\sigma_0} - 1 = \frac{s_o^2\cos^4\theta_0}{(s_o^2 + \delta s^2)\cos^4(\theta_o + \delta\theta)} \frac{\exp\left(\dfrac{\tan^2\theta_0}{s_0^2}\right)}{\exp\left(\dfrac{\tan^2(\theta_o + \delta\theta)}{s_o^2 + \delta s^2}\right)} - 1 \tag{8}$$

with the square tangent of the disturbed incidence angle:

$$\tan^2\delta\theta = +\delta s^2, \qquad \frac{\partial u_{perp}}{\partial x_{perp}} \le 0 \tag{9a}$$

$$-\tan^2\delta\theta = -\delta s^2, \qquad \frac{\partial u_{perp}}{\partial x_{perp}} > 0 \tag{9b}$$

and the disturbed square slope:
$$\delta s^2 = \int_{k_o}^{k_c} \vec{k}^2(\vec{x})\,\delta F(\vec{x},\vec{k})\,\mathrm{d}\vec{k} \tag{10}$$

where x_{perp} is the space variable defined perpendicular to the sand wave crest (Figure 3), $\vec{k}$ is the wave number vector of short gravity waves, k_o is the lower limit of the wave number producing quasi-specular scattering modulation, k_c is the maximum wave number at which the effect of surface tension is negligible, $\partial u_{perp}/\partial x_{perp}$ is the gradient or strain rate of the current velocity perpendicular to the sand wave crest (Figure 3), and $\delta F(\vec{x},\vec{k})$ is the perturbation term of the wave-energy density spectrum in the short gravity wave regime caused by wave-current interaction applying weak hydrodynamic interaction theory (19). The perturbation term $\delta F(\vec{x},\vec{k})$ can be interpreted as the density of contributions to δs^2 per unit area of $\vec{k}$ space. The spatial scale of the waves re-

sponsible for the quasi-specular scattering modulation was assumed to be in the range of wave-lengths $\lambda_c = 2\pi/k_c = 0.032$ m and $\lambda_o = 2\pi/k_o = 7.5$ m. These values have been selected because the microwave wavelength of the radar is $\lambda_{radar} = 0.032$ m and the spatial resolution of the radar is $\rho_{radar} = 7.5$ m. The parameters $\delta\theta$ and δs^2 expressed by Eqs. (9)-(10) are defined positive as well as negative depending on the sign of the current gradient or strain rate $\partial u_{perp}/\partial x_{perp}$. Short surface waves are stretched within a divergent current regime and the square tangent of the local inci-dence angle and the total variance of local slopes are reduced from equilibrium due to a dimin-ished wave height spectrum $\psi(\vec{k})$ or wave-energy density spectrum $F(\vec{k})$. On the other hand short surface waves are compressed within a convergent current regime where the square tangent of the local incidence angle and the total variance of local slopes are enhanced from equilibrium due to an increased wave height spectrum $\psi(\vec{k})$ or wave-energy density spectrum $F(\vec{k})$. To derive Eq. (10) the relationship shown by (20) has been used where the mean square slope of sea sur-face waves is obtained from the wave height spectrum $\psi(\vec{k})$ or wave-energy density spectrum $F(\vec{k})$ of ocean gravity waves:

$$s^2 = \int k^2 F(\vec{k})\, d\vec{k} \tag{11}$$

The integration should cover the possible range of the wave number. Considering Eq. (11) statisti-cally this relation is also the common definition of the variance of a continuously distribution func-tion. The relationship between $\psi(\vec{k})$, $F(\vec{k})$ and the wave action density spectrum

$$N(\vec{k}) = F(\vec{k})\,(\omega'(k))^{-1}$$

is defined by (21):
$$F(\vec{k}) = \omega'(\vec{k})\,N(\vec{k}) = \frac{(\omega'(\vec{k}))^2}{k}\,\psi(\vec{k}) \tag{12}$$

with the wave height spectrum
$$\psi(k) = a_P k^{-4} \tag{13}$$

where a_P is known as the Phillips constant. Due to measurements by (22), the empirical relation for a_P as a function of wind speed $U_w \le 8$ m s^{-1} is used:

$$\log_{10} a_p = -2.90 + 3.06 \cdot 10^{-1} U_w - 1.85 \cdot 10^{-2} U_w^2 \tag{14}$$

The dispersion relation for gravity waves in equation (12) is defined by:

$$\omega' = (gk)^{1/2} \tag{15}$$

For the modulation of the first order perturbed wave-energy density spectrum $\delta F/F_o = (F-F_o)/F_o$ (with F_o as the unperturbed wave-energy density spectrum) the expression derived by (6) is used:

$$\frac{\delta F}{F_o} = -4.5 \frac{\partial u_{perp}}{\partial x_{perp}} \left((\vec{c}_g + \vec{u}_o)\,\frac{1}{L} + \mu \right)^{-1} \tag{16}$$

with the absolute value of the group velocity for gravity waves:

$$|\vec{c}_g| = \frac{1}{2}\frac{\omega'}{k} \tag{17}$$

where $\vec{u}_o$ is the mean current velocity of the undisturbed sea area, μ is the relaxation rate parame-ter, g is the acceleration of gravity, and L denotes the length scale of the slope of the bed form. The length scale of the slope L is different for asymmetric sand waves as shown in Figure 3; $L = L_{SSL}$ is the length scale of the steep slope and $L = L_{GSL}$ is the length scale of the gentle slope of the sand wave, respectively.

The result of Eq. (16) is derived by using the action balance or radiation balance equation based on the weak hydrodynamic interaction theory according to (19). This transport equation describes the variation of the spectral energy density of short waves in a slowly varying current field. It implies that a slowly varying surface current is able to create only small magnitudes of the disturbed square slope. These conditions are often not fulfilled within a strong current gradient caused by large slopes of marine sand waves. On the other hand according to the weak hydrodynamic interaction theory it is sufficient that the strain rate should be much less than the radian frequency of short surface water waves. This condition has been fulfilled during the OROMA experiments (see subsection on "Measured and simulated NRCS modulations").

METHODS

Several field experiments of the *Operational Radar and Optical Mapping in monitoring hydrodynamic, morphodynamic and environmental parameters for coastal management project* (OROMA) of the Fifth Framework Programme of the European Commission (EC) have been carried out during 2002-2004. One of the study areas is the Lister Tief, a tidal inlet of the German Bight in the North Sea bounded by the islands of Sylt to the south and Rømø to the north, respectively, as shown in Figures 1a-c. The OROMA experiments took place in the sea area of the Lister Tief marked by the parallelogram in Figure 1c. The measurements performed during the period 6-23 September 2004 on board the Research Vessel (R.V.) *Ludwig Prandtl* of the GKSS Research Centre, Geesthacht, Germany, will be described here.

The Lister Tief was selected because one of the most pronounced and dynamic marine sand wave fields in German coastal waters is located in this tidal channel. R.V. *Ludwig Prandtl* was equipped with the following sensors: a Parametric Sediment Echo Sounder SES-2000 with a frequency of 12 kHz, a Precise Differential Global Positioning System (PDGPS), an RD Instruments Acoustic Doppler Current Profiler (ADCP) with 4 downward-looking convex transducers using an incidence angle of 20° and a frequency of 1200 kHz, a Kelvin Hughes RSR 1000 X-band VV polarized river radar with a frequency of 9.42 GHz, a Siggelkow Gerätebau GmbH Soni 3 meteorological sensor system, a ME Ecosonde Conductivity-Temperature-Depth (CTD) probe, and handheld cameras.

Current velocity profiles were measured using the ADCP. Almost all surveying profiles of the ADCP measurements across the study area were obtained on board R.V. *Ludwig Prandtl* at a ship speed between 1.5 m s^{-1} and 4.5 m s^{-1}. The ADCP was mounted within the moon pool of the ship at 1.7 m water depth. Bottom tracking is implemented. The current velocity measurements were recorded continuously from a water depth 2.32 m below the sea surface to 1.2 m above the sea bed, separated into water depth cells (bins) of 0.25 m. At the bottom interface the ADCP data have to be considered with caution due to acoustic interference from the bottom. The collected and processed data after each pulse transmission have been averaged over a sampling interval of five seconds. At the end of the sampling interval, a profile of the resulting current velocity relative to the ADCP was generated as a function of range and then stored on the hard disk of the connected computer. The relative accuracy of the current velocity is ± 1 cm s^{-1} and the accuracy of the estimated absolute current velocity is ± 5 cm s^{-1}.

The important progress realised within the OROMA project is the availability of calibrated shipborne X-band radar data. NRCS modulation data were measured and mapped during ebb and flood tidal current phases, respectively. The backscattered radar signals from the water surface were received by a fixed antenna (not a rotating one) using the so- called radar scanning mode. This kind of mode is comparable to the acoustic side-scan imaging mode used by sonar and multibeam echo sounders. The profiles were arranged in such a way that the R.V. *Ludwig Prandtl* followed approximately the orientations of the sand wave crests. The look direction of the radar antenna was perpendicular to the profiles expecting the most useful NRCS modulation signatures caused by marine sand waves. The distance of the profiles was 100 m. Radar data from a ground range of 562.5 m beginning at a distance of 112.5 m from the foot point of the antenna at the sea surface perpendicular to the ship track have been further processed.
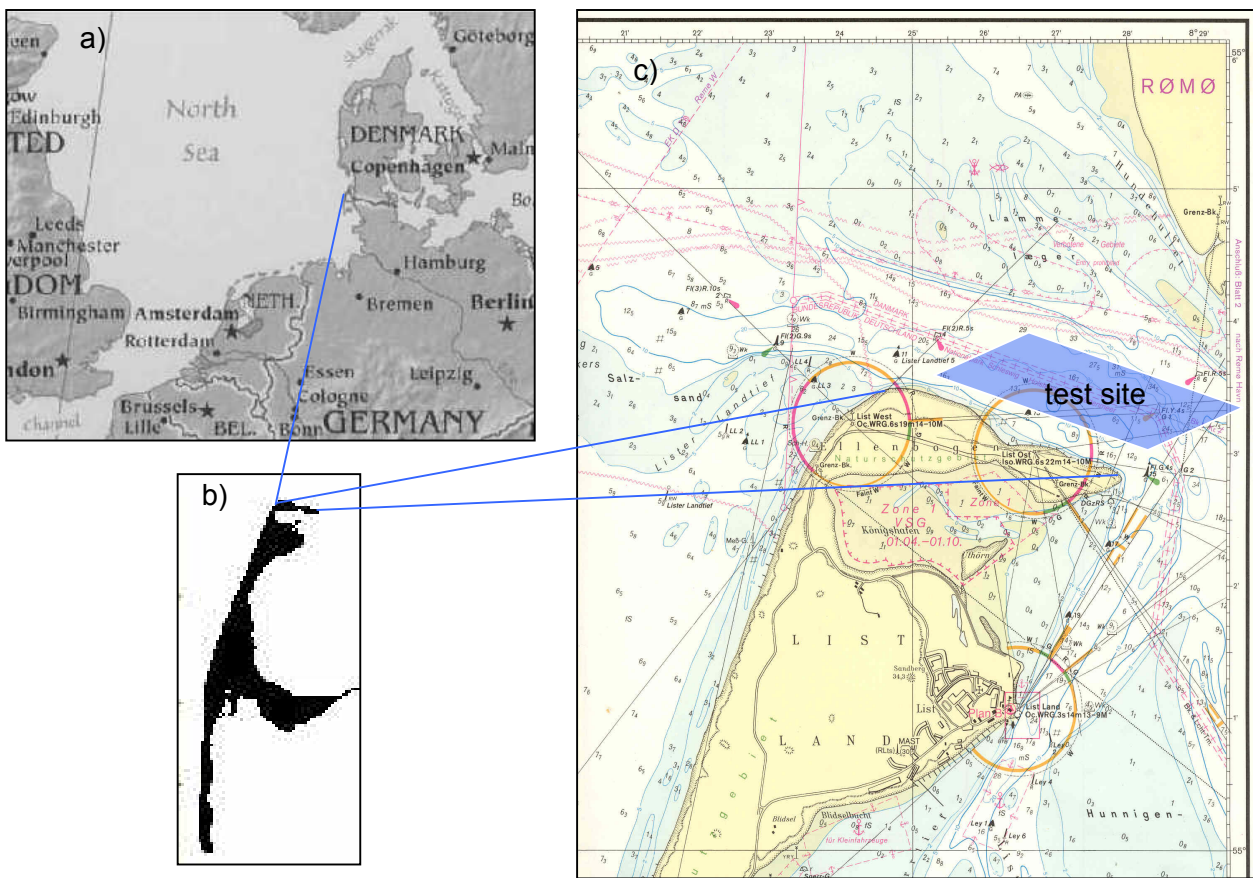
Figure 1: a-b) Locations of the island of Sylt and the Lister Tief in the German Bight of the North Sea; c) Bathymetry of the Lister Tief tidal channel bounded by the islands of Sylt to the south and Rømø to the north. The OROMA experiments were carried out in the sea area of the Lister Tief marked by the parallelogram.

RESULTS

Sea bottom topography and mesoscale dynamics

Marine sand waves are one of the most conspicuous natural phenomena, especially from a sedimentological point of view. The internal structure, dynamics and morphology of marine sand waves as well as their associated hydrodynamic processes are the subject of several current research activities (23).

In this section the behaviour of large asymmetrical sand waves (width: 100-350 m) with large lee slopes (≤ 31°) and associated mega ripples (width: 0.5-2 m) located in the troughs of sand waves will be outlined. A pre-processed map of the sea bottom topography of the whole study area in the Lister Tief as recorded during the OROMA experiment in September 2004 is shown in Figure 2. Sounding tracks at 50 m distances were gathered by the SES-2000 echo sounder in combination with a PDGPS system. The transducer system of the SES-2000 echo sounder system was installed within the R.V. *Ludwig Prandtl* nearly below the PDGPS antenna. The data triplets (x,y,z), with x and y the two horizontal and z the vertical space coordinates, respectively, have been interpolated onto a grid of 7.5 m by 7.5 m and is visualized on a map based on Gauss-Krüger-Coordinates (GK) in Fig. 2. The coverage is 3850 m by 1350 m. The location of the NRCS modulation image visualised in Figure 4 is marked by A and the profiles of simulated and measured NRCS modulations due to asymmetric sand waves presented in Figures 5-6 are marked by BB' and CC', respectively, in Figure 2.
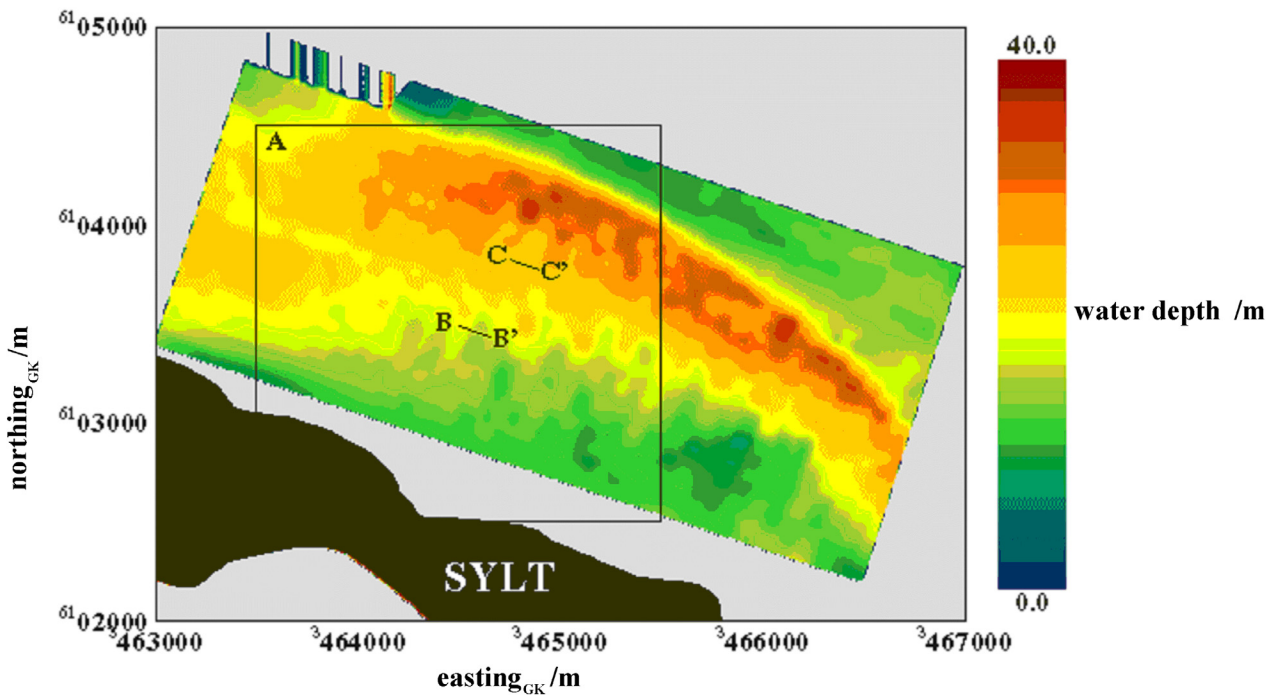
Figure 2: Pre-processed map of the sea bottom topography of the whole study area in the Lister Tief as recorded by the SES-2000 echo sounder in combination with the Precise Differential Global Positioning System (PDGPS) during the OROMA experiment in September 2004. The data were interpolated onto a grid of 7.5 m by 7.5 m and are visualised in a map based on Gauss-Krüger-Coordinates (GK). The location of the NRCS modulation image visualized in Figure 4 is marked by A and the profiles of simulated and measured NRCS modulations due to asymmetric sand waves presented in Figures 5-6 are marked by BB' and CC', respectively.

The sea bed morphology of the Lister Tief tidal channel is a complex configuration of different bed-forms. The marine sand waves investigated in this study are four-dimensional in space and time. Small-scale as well as mega-ripples are superimposed on sand waves. In the troughs of sand waves often mega-ripple fans can be observed with a crest orientation perpendicular to the orientation of sand waves. The sand waves have heights ≤ 11 m and often crest to crest distances (widths) ≥ 300 m. In the past, systematic morphological investigations have been carried out to study the migration of these sand waves (18). In the northern section of the test area most of the sand waves have ebb tide oriented forms; in the southern part most of them are flood tide oriented. In the south-eastern part the stoss slopes of sand waves are of the order of $\partial z/\partial x \leq 0.017$ (1°). The lee slopes have maximum values of $\partial z/\partial x = 0.591$ (30.6°). Data analysed by (18) showed that sand waves with a mean height of 3 m migrated about 60 m per year. During the OROMA experiments flood tide oriented sand waves migrated 80 m per year from west to east according to echo sounding measurements.

Experimental and field investigations of sand waves have documented turbulent events called "kolks" and "boils" (24,25). The so called "kolk-boil" mechanism is one of predominant turbulent events occurring over sand waves in fluvial, estuarine, and marine coastal environments (26). A kolk is a slowly rotating, upward-tilting vortex on the stoss face of a sub aqueous bedform. A strong kolk may reach the water surface, can create a cloudy columnar sediment-fluid mixture, and form a raised circular or oval patch at the air-water interface, referred to as a boil (24,27). These boils are created on a scale which is comparable to the flow depth itself as a first approximation. This mechanism is visualised by so-called "waterspouts", the upward orientated component u_{vert} of the three-dimensional current velocity field measured by the ADCP at the stoss faces of asymmetric marine sand waves in the Lister Tief (28). The waterspouts were measured by the ADCP of the same kind during ebb and flood tidal current phases, respectively. During the ebb tidal phase the waterspouts are upwelling events and during flood tidal phase they are associated with downwel-

ling at the steep flanks of the investigated marine sand waves. The origin of the kolk at the stoss side of the sand wave is located at the reattachment point (Figure 3). The schematic sketch of sand wave-related mesoscale dynamics caused by ebb tidal currents over flood-tide oriented sand waves, the associated secondary circulation regimes described above, as well as coordinate systems and definition of symbols used in the next section are visualised in Figure 3.
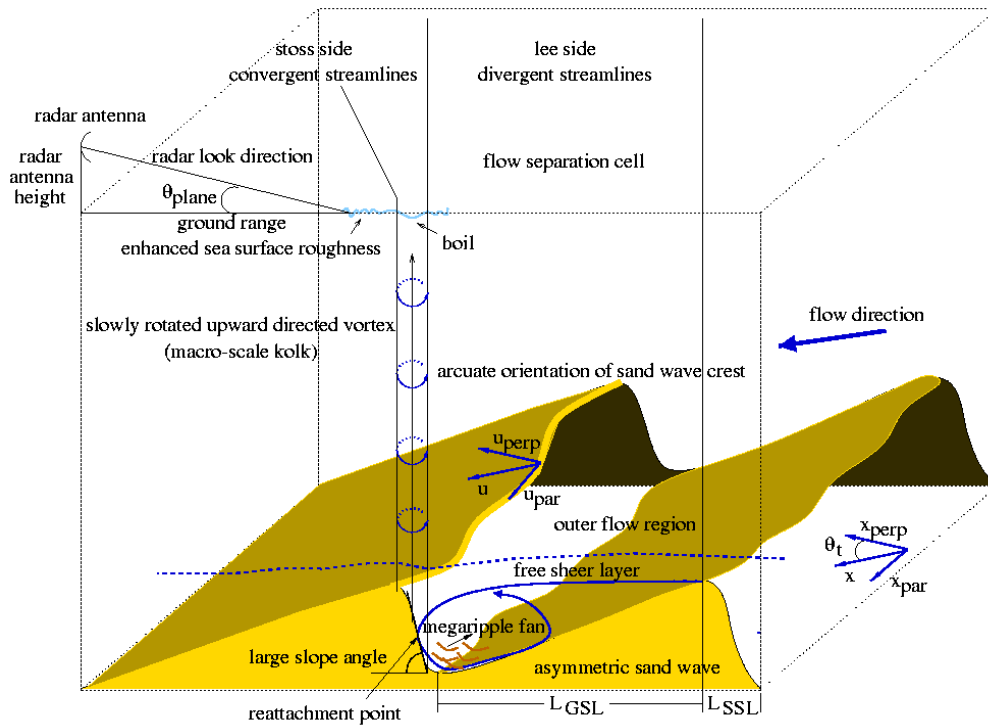

Figure 3: Schematic sketch of the characteristic fluid flow in the water column, the mesoscale dynamics and the macro turbulence mechanism caused by ebb tidal currents over flood tide oriented marine sand waves, as well as coordinate systems and definition of symbols used in the subsection describing the theory.

Measured and simulated NRCS modulations

A composite of 23 single radar images taken at 0800-1325 UTC 07 September 2004 in the sea area of the Lister Tief during ebb tidal current phase is shown in Figure 4. The location of the radar image is marked as a frame indicated by A in Figure 2. At the acquisition time intervals of the radar composite wind speeds between 4.0 m s^{-1} and 7.5 m s^{-1} from easterly directions were measured. The NRCS modulation shown in Figure 4 is dominated by bright signatures of asymmetric ebb as well as flood-tide oriented marine sand waves. Enhanced roughness patterns (bright signatures) are located within the convergent zones of the tidal current gradient above the slopes of sand waves as indicated in Figure 3. The NRCS modulations show also a variation along the signatures itself. This is indeed reflected by the 3-D marine sand waves shown in Figure 2.

During the OROMA experiments it was not possible to take all measurements from on board the R.V. *Ludwig Prandtl* parallel and normal to the sand wave crests quasi simultaneously. But both are needed according to the theory presented. The water depth and current velocity data gathered at 1001-1002 UTC 06 September 2004 and at 1203-1204 UTC 06 September 2004, respectively, are oriented normal to the sand wave crests. The radar profiles of measured NRCS data were taken at 0826-0836 UTC 07 September 2004 and are oriented parallel to the sand wave crests. All data sets have been acquired during ebb tidal current phase and under comparable wind speed and wind direction conditions. Therefore, both data sets have been merged. Results are presented

for a flood tide as well as for an ebb tide oriented marine sand wave in Figures 5 and 6, respectively.
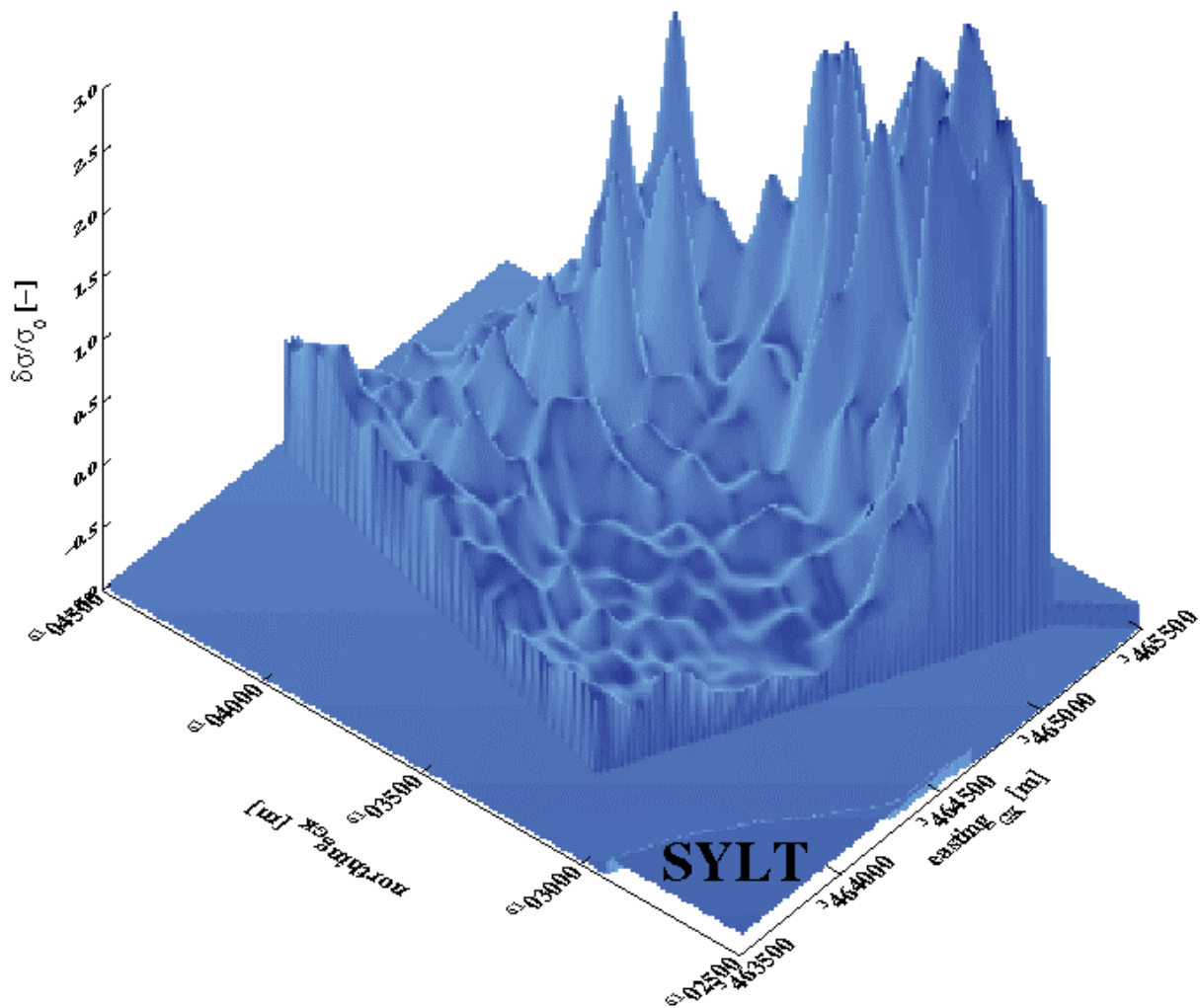

Figure 4: NRCS modulation composite of 23 single radar images taken at 0800-1325 UTC 07 September 2004 from on board the R.V. Ludwig Prandtl in the sea area of the Lister Tief during ebb tidal current phase. The location of the NRCS modulation composite is marked as a frame indicated by A in Figure 2. The NRCS modulation imaged as bright signatures is caused by asymmetric ebb and flood tide oriented marine sand waves.

The positions of the first analysed water depth profile which is identical with the ADCP profile marked by BB' in Figure 2 as well as the measured NRCS modulation profile based on GK-coordinates are shown in Figure 5a. The water depth as a function of position is presented in Figure 5b. This flood tide oriented sand wave has a width of 155.1 m and a height of 4.19 m. The mean vertical integrated current speed u_{perp} perpendicular to the sand wave crest is presented in Figure 5c. A maximum current speed of $u_{perp}^{max} = 0.59$ m s^{-1} was measured at the crest of the sand wave. The variation of the current speed between the trough and crest of the sand wave is $\Delta u_{perp} = 0.09$ m s^{-1}. Figure 5d shows the strain rate or the gradient of the perpendicular component relative to the sand wave crest of the current velocity $\partial u_{perp}/\partial x_{perp}$ using the measured ADCP data presented in Figure 5c. These data show the typical distribution of divergent and convergent flow patterns associated with asymmetrical sand waves and confirms the theory developed by (6). Minimum and maximum values of the strain rate of -0.0015 s^{-1} and 0.0015 s^{-1} have been calculated.
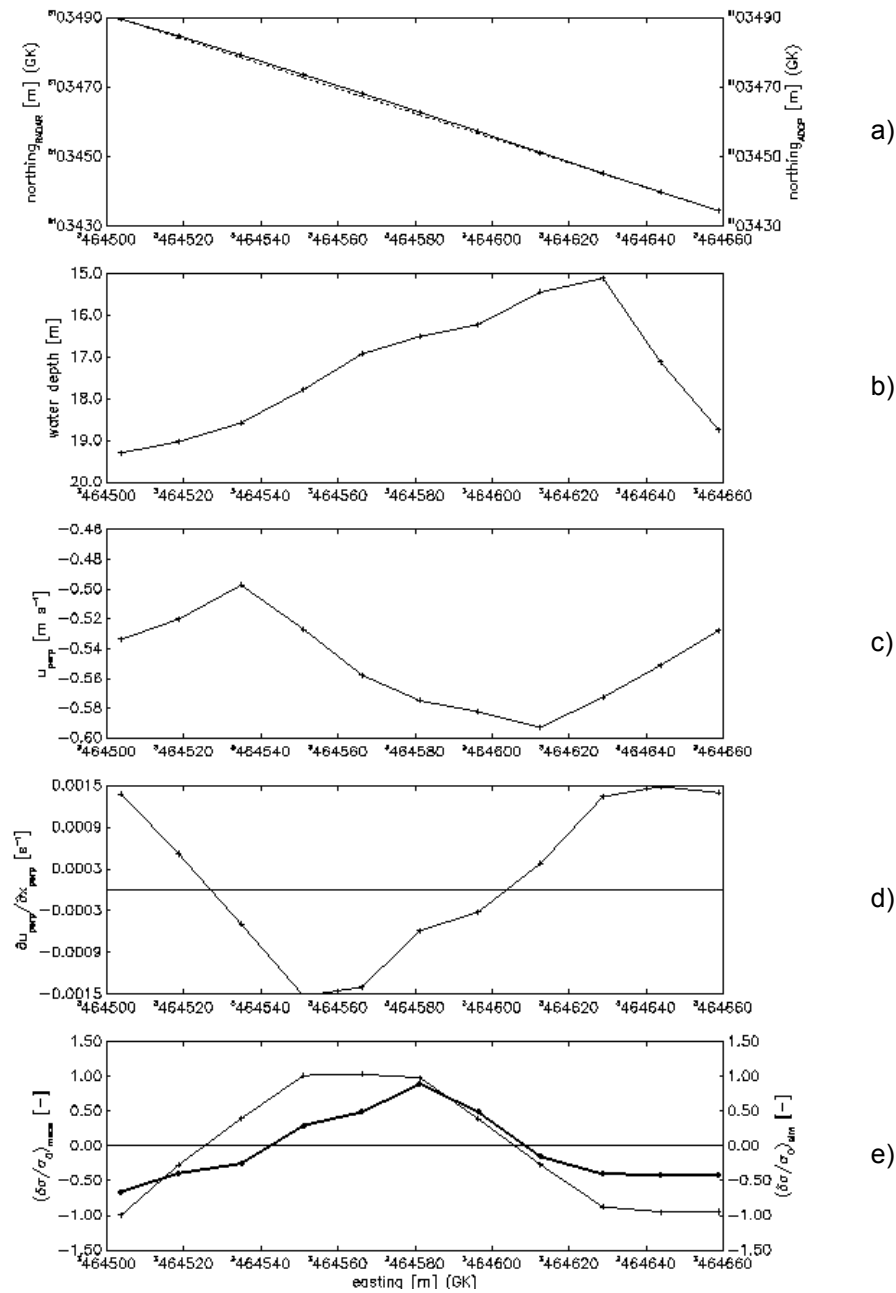
Figure 5: Analysed echo sounder and ADCP data taken at 1001-1002 UTC 06 September 2004 and measured radar data taken at 0826-0836 UTC 07 September 2004 during ebb tidal phase for the flood tide oriented marine sand wave; a) Positions of the analysed water depth and ADCP profile (northing$_{ADCP}$, solid line, marked by BB' in Figure 2) as well as measured NRCS modulation profile (northing$_{RADAR}$, broken line) based on Gauss-Krüger-Coordinates (GK); b) water depth as a function of position; c) mean vertical integrated current speed u$_{perp}$ perpendicular to the sand wave crest as a function of position; d) strain rate or gradient of the perpendicular component relative to the sand wave crest of the current velocity $\partial u_{perp}/\partial x_{perp}$ as a function of position; e) simulated NRCS modulation ($\delta\sigma/\sigma_o$)$_{sim}$ applying Eq. (8) (solid thin line) and measured NRCS modulation ($\delta\sigma/\sigma_o$)$_{meas}$ (solid thick line) as a function of position.
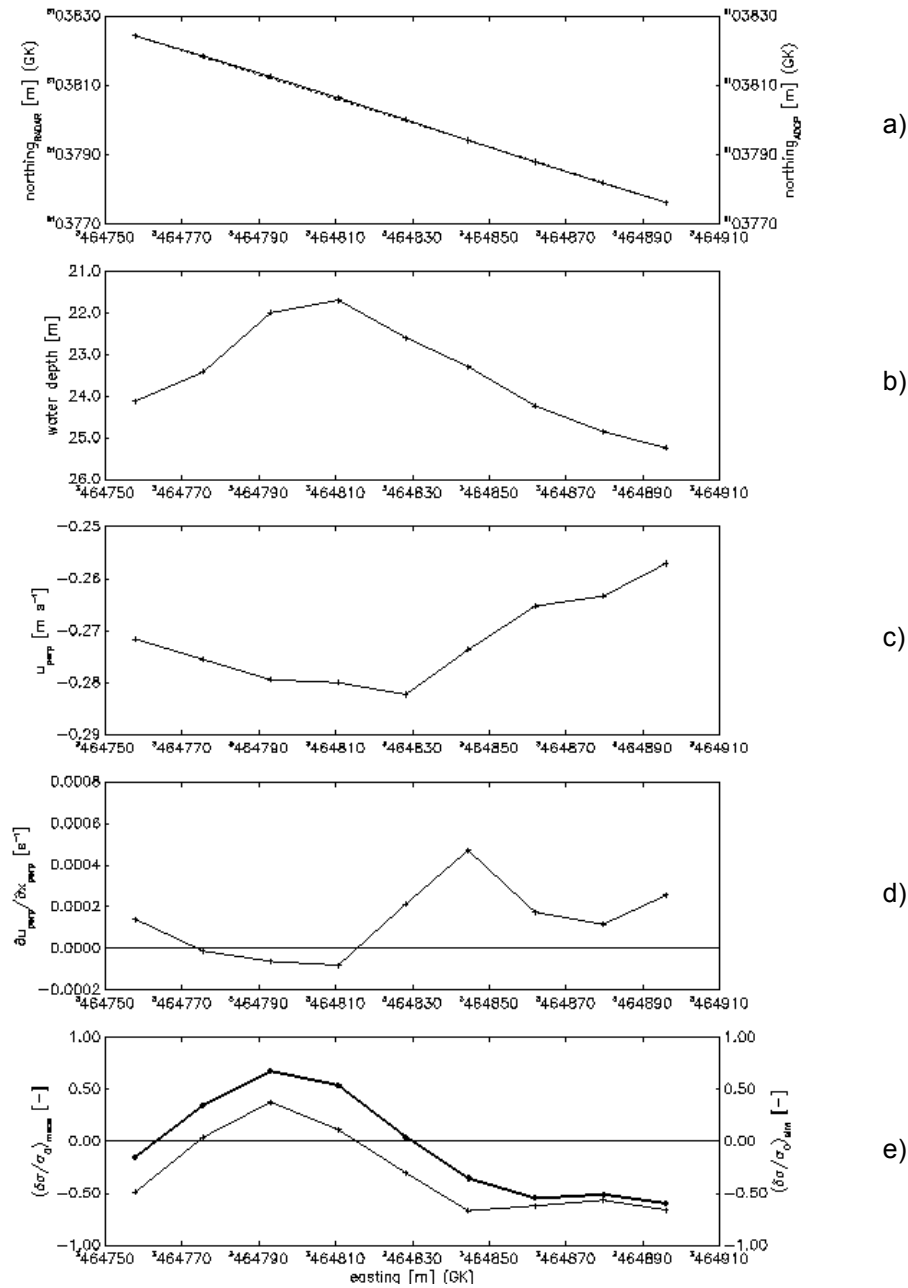
Figure 6: Analysed echo sounder and ADCP data taken at 1203-1204 UTC 06 September 2004 and measured radar data taken at 0826-0836 UTC 07 September 2004 during ebb tidal phase for the ebb tide oriented marine sand wave; a) Positions of the analysed water depth and ADCP profile (northing$_{ADCP}$, solid line, marked by CC' in Fig. 2) as well as the measured NRCS modulation profile (northing$_{RADAR}$, broken line) based on Gauss-Krüger-Coordinates (GK); b) water depth as a function of position; c) mean vertical integrated current speed u$_{perp}$ perpendicular to the sand wave crest as a function of position; d) strain rate or gradient of the perpendicular component relative to the sand wave crest of the current velocity $\partial u_{perp}/\partial x_{perp}$ as a function of position; e) simulated NRCS modulation ($\delta\sigma/\sigma_0)_{sim}$ applying Eq. (8) (solid thin line) and measured NRCS modulation ($\delta\sigma/\sigma_0)_{meas}$ (solid thick line) as a function of position.

The comparison of simulated NRCS modulation ($\delta\sigma/\sigma_0)_{sim}$ with measured NRCS modulation ($\delta\sigma/\sigma_0)_{meas}$ as a function of position is shown in Figure 5e. The calculations for ($\delta\sigma/\sigma_0)_{sim}$ using Eq. (8) are carried out for $k_o = 2\pi/\lambda_o = 0.84\,\text{m}^{-1} \leq k \leq k_c = 2\pi/\lambda_{radar} = 196.35\,\text{m}^{-1}$, $g = 9.81\,\text{ms}^{-2}$, $|\vec{u}_o| = 0.40\,\text{m s}^{-1}$, L_{SSL} = 30 m, L_{GSL} = 125.1 m, μ = 0.051 s^{-1}, U_w = 4.5 m s^{-1} with an easterly wind direction coming from 92.10°, and θ_{plane} = 1.3°. The value for μ has been obtained by measure-

ments derived by (29). For the current gradient $\partial u_{perp}/\partial x_{perp}$ the data based on ADCP measurements shown in Figure 5d have been used for $(\delta\sigma/\sigma_o)_{sim}$. The simulated NRCS modulation $(\delta\sigma/\sigma_o)_{sim}$ presented in Figure 5e shows a maximum modulation $(\delta\sigma/\sigma_o)_{sim}^{max} = 1.05$ at the gentle slope of the sand wave. The measured maximum NRCS modulation $(\delta\sigma/\sigma_o)_{meas}^{max} = 0.84$ is located also at the gentle slope of the sand wave but with a distinct offset of 15 m in upstream direction of the tidal current. The value of the measured minimum modulation $(\delta\sigma/\sigma_o)_{meas}^{min} = -0.50$ in the divergent region at the steep slope of the sand wave is lower than the value of the simulated modulation $(\delta\sigma/\sigma_o)_{sim}^{min} = -0.93$.

The positions of the second analysed water depth profile which is identical with the ADCP profile marked by CC' in Figure 2 as well as the measured NRCS modulation profile based on GK-coordinates are shown in Figure 6a. Water depth as a function of position is shown in Figure 6b. This ebb tide oriented sand wave has a width of 138.2 m and a height of 3.55 m. The mean vertical integrated current speed u_{perp} perpendicular to the sand wave crest is presented in Figure 6c. A maximum current speed $u_{perp}^{max} = 0.28\,\text{m s}^{-1}$ has been measured at the crest of the sand wave. The variation of the current speed between the trough and crest of the sand wave is $\Delta u_{perp} = 0.02\,\text{m s}^{-1}$. The strain rate or gradient of the perpendicular component relative to the sand wave crest of the current velocity $\partial u_{perp}/\partial x_{perp}$ is shown in Figure 6d. Minimum and maximum values of the strain rate of -0.0001 s^{-1} and 0.0005 s^{-1} have been calculated. The comparison of simulated NRCS modulation $(\delta\sigma/\sigma_o)_{sim}$ with measured NRCS modulation $(\delta\sigma/\sigma_o)_{meas}$ as a function of position is shown in Figure 6e. The calculations for $(\delta\sigma/\sigma_o)_{sim}$ applying Eq. (8) are carried out for $k_o = 2\pi/\lambda_o = 0.84\,\text{m}^{-1} \le k \le k_c = 2\pi/\lambda_{radar} = 196.35\,\text{m}^{-1}$, $g = 9.81\,\text{m s}^{-2}$, $|\bar{u}_o| = 0.27\,\text{m s}^{-1}$, $L_{SSL} = 52.9\,\text{m}$, $L_{GSL} = 85.3\,\text{m}$, $\mu = 0.050\,\text{s}^{-1}$ (according to (29)), U_w = 3.9 m s^{-1} with an easterly wind direction of 118.24°, and θ_{plane} = 2.6°. For the current gradient $\partial u_{perp}/\partial x_{perp}$ the data based on ADCP measurements shown in Figure 6d have been used for the simulation of $(\delta\sigma/\sigma_o)_{sim}$. The simulated NRCS modulation $(\delta\sigma/\sigma_o)_{sim}$ shows a maximum modulation $(\delta\sigma/\sigma_o)_{sim}^{max} = 0.39$ at the steep slope of the sand wave and also the measured maximum NRCS modulation $(\delta\sigma/\sigma_o)_{meas}^{max} = 0.66$ is located at the same position. However, the value of the measured minimum modulation $(\delta\sigma/\sigma_o)_{meas}^{min} = -0.60$ at the easterly divergent region associated with the gentle slope of the sand wave is somewhat lower than the simulated one $(\delta\sigma/\sigma_o)_{sim}^{min}$ = -0.70.

DISCUSSION AND CONCLUSIONS

Radar signatures of sea bottom topography are dominated by the Bragg scattering theory since most of the imaging radars operate at incidence angles between 20° and 70° (17). A radar scattering theory of NRCS modulation caused by submarine bedforms at very low grazing angle illumination generally accepted by the scientific community still does not exist until now. However, new monitoring technologies such as shore- and shipborne imaging radars applied for coastal monitoring purposes are becoming more and more important. This subject was the main motivation to investigate if the quasi-specular scattering theory can be applied at a very low grazing angle to explain the X-band radar imaging mechanism of marine sand waves. The theoretical model presented here is not capable of explaining all aspects of the NRCS modulation due to marine sand waves quantitatively. Nevertheless, it is proposed that the quasi-specular scattering theory at a very low grazing angle is a first-order theory because the results of the simulated NRCS modulation show the qualitative trend, but do not always quantitatively match the measured NRCS modulation profiles. According to the Bragg scattering theory, the NRCS for small water surface waves is proportional to the wave height spectral density $\psi(\vec{k})$ at the Bragg backscatter wave numbers. For quasi-specular scattering theory from a rough ocean surface, the NRCS is proportional to the total variance of slopes created by ocean surface waves. The relaxation rate μ is one of the most crucial parameters in weak hydrodynamic interaction theory and has to be taken into consideration when

applying the presented theory. Comprehensive discussions concerning μ have been published by (29,30). Another crucial point was the scarce availability of calibrated NRCS data based on nautical ship radars. Within the OROMA project calibrated shipborne X-band radar data were made available and have been compared with simulated NRCS modulation data. First comparisons of simulated and measured NRCS modulations show encouraging results, but should be treated with some caution because NRCS and current velocity could not be measured simultaneously within the experimental set up. Simultaneously measured ADCP and NRCS data are needed, because the current gradient or strain rate is one of the most important parameters of the applied weak hydrodynamic interaction theory. A new measurement configuration concerning this aspect has to be reflected on for future experiments.

From the results derived in this paper the following conclusions can be drawn for the X-band radar imaging mechanism at very low grazing angles $\leq 15°$ of flood and ebb tide oriented sand waves during ebb tidal current phase for wind speeds ≤ 8 m s^{-1} and water depths ≤ 50 m:

1. The simulated NRCS modulation $(\delta\sigma/\sigma_o)_{sim}$ and the measured NRCS modulation $(\delta\sigma/\sigma_o)_{meas}$ have the same order of magnitude; the difference between $(\delta\sigma/\sigma_o)_{sim}^{max}$ and $(\delta\sigma/\sigma_o)_{meas}^{max}$ of the ebb tide oriented sand wave is 27% and the difference between $(\delta\sigma/\sigma_o)_{sim}^{max}$ and $(\delta\sigma/\sigma_o)_{meas}^{max}$ of the flood tide oriented sand wave is 21%, respectively. The difference between $(\delta\sigma/\sigma_o)_{sim}^{min}$ and $(\delta\sigma/\sigma_o)_{meas}^{min}$ of the ebb tide oriented sand wave is 10% and the difference between $(\delta\sigma/\sigma_o)_{sim}^{min}$ and $(\delta\sigma/\sigma_o)_{meas}^{min}$ of the flood tide oriented sand wave is 43%, respectively. These results are acceptable but have to be improved.

2. The phases of simulated and measured NRCS modulations are correlated with the slopes of asymmetric sand waves. The phases of $(\delta\sigma/\sigma_o)_{sim}^{max}$ and $(\delta\sigma/\sigma_o)_{meas}^{min}$ of the ebb tide oriented sand wave coincide fairly well; on the other hand only the phases of $(\delta\sigma/\sigma_o)_{sim}^{min}$ and $(\delta\sigma/\sigma_o)_{meas}^{min}$ of the flood tide oriented sand wave coincide, where the phases between $(\delta\sigma/\sigma_o)_{sim}^{max}$ and $(\delta\sigma/\sigma_o)_{meas}^{max}$ show a difference in position of 15 m.

3. The magnitudes of the simulated and measured NRCS modulations of the ebb tide oriented sand wave are significantly lower than the magnitudes of the flood tide oriented sand wave. This is consistent with the theory because the strain rate is significantly lower for the ebb tide oriented sand wave.

ACKNOWLEDGEMENTS

REFERENCES

1   McLeish W, D J P Swift, R B Long, D Ross & G Merrill, 1981. Ocean surface patterns above sea-floor bedforms as recorded by radar, southern bight of North Sea. Marine Geology, 43: M1-M8

2   Hennings I, S Stolte & F Ziemer, 1994. Experimental method to measure surface signature generation by sea bottom undulations. IEEE Journal of Oceanic Engineering, 19: 36-40

3   Vogelzang J, G J Wensink, C J Calkoen & M W E Van der Kooij, 1997. Mapping submarine sandwaves with multi-band imaging radar 2. Experimental results and model comparison. <u>Journal of Geophysical Research</u>, 102(C6): 1183-1192

4   Lamont-Smith T, A M Jackson, P W Shepherd & R D Hill, 2005. Low grazing angle radar imaging experiments over the South Falls sandbank. <u>International Journal of Remote Sensing</u>, in press

5   De Loor G P, 1981. The observation of tidal patterns, currents and bathymetry with SLAR imagery of the sea. <u>IEEE Journal of Oceanic Engineering</u>, 6: 124-129

6   Alpers W & I Hennings, 1984. A theory of the imaging mechanism of underwater bottom topography by real and synthetic aperture radar. <u>Journal of Geophysical Research</u>, 89(C6): 10529-10546

7   Shuchman R A, D R Lyzenga & G A Meadows, 1985. Synthetic aperture radar imaging of ocean-bottom topography via tidal-currents interactions: theory and observations. <u>International Journal of Remote Sensing</u>, 6: 1179-1200

8   Phillips O M, 1984. On the response of short ocean wave components at a fixed wavenumber to ocean current variations. <u>Journal of Physical Oceanography</u>, 14: 1425-1433

9   Zimmerman J F T, 1985. Radar images of the sea bed. <u>Nature</u>, 314: 224-226

10 Hennings I, 1990. Radar imaging of submarine sand waves in tidal channels. <u>Journal of Geophysical Research</u>, 95(C6): 9713-9721

11 Romeiser R & W Alpers, 1997. An improved composite surface model for the radar backscattering cross section of the ocean surface. 2. Model response to surface roughness variations and the radar imaging of underwater bottom topography. <u>Journal of Geophysical Research</u>, 102(C6): 25251-25267

12 Vogelzang J, 1997. Mapping submarine sandwaves with multi-band imaging radar 1. Model development and sensitivity analysis. <u>Journal of Geophysical Research</u>, 102(C6): 1163-1181

13 Hennings I, 1998. An historical overview of radar imagery of sea bottom topography. <u>International Journal of Remote Sensing</u>, 19: 1447-1454

14 Hesselmans G H F M, G J Wensink, C G Van Koppen, C Vernemmen & C Van Cauwenberghe, 2000. Bathymetry assessment demonstration off the Belgian coast - BABEL. <u>The Hydrographic Journal</u>, 96: 3-8

15 Calkoen C J, G H F M Hesselmans, G J Wensink & J Vogelzang, 2001. The bathymetry assessment system: efficient depth mapping in shallow seas using radar images. <u>International Journal of Remote Sensing</u>, 22: 2973-2998

16 Inglada J & R Garello, 2002. On rewriting the imaging mechanism of underwater bottom topography by synthetic aperture radar as a Volterra series expansion. <u>IEEE Journal of Oceanic Engineering</u>, 27: 665-674

17 Valenzuela G R, 1978. Theories for the interaction of electromagnetic and ocean waves - A review. <u>Boundary-Layer Meteorology</u>, 13: 277-293

18 Cox C & W Munk, 1954. Measurement of the roughness of the sea surface from photographs of the sun's glitter. <u>Journal of the Optical Society of America</u>, 44: 838-850

19 Alpers W & K Hasselmann, 1978. The two-frequency microwave technique for measuring ocean wave spectra from an airplane or satellite. <u>Boundary Layer Meteorology</u>, 13: 215-230

20 Phillips O M, 1977. <u>The dynamics of the upper ocean</u> (Cambridge University Press) 343 pp.

21 Holliday D, G St-Cyr & N E Woods, 1986. A radar ocean imaging model for small to moderate incidence angles. International Journal of Remote Sensing, 7: 1809-1834

22 Stolte S, 1990. Dynamics of short waves and wave breaking (Federal Armed Forces Underwater Acoustics and Marine Geophysics Research Institute Kiel) Report 1990-4, 48 pp.

23 Le Bot S & A Trentesaux, 2004. Types of internal structure and external morphology of submarine dunes under the influence of tide- and wind-driven processes (Dover Strait, northern France). Marine Geology, 211: 143-168

24 Matthes G H, 1947. Macroturbulence in natural stream flow. Transactions American Geophysical Union, 28: 255-262

25 Coleman J M, 1969. Brahmaputra River: channel processes and sedimentation. Sedimentary Geology, 3: 129-239

26 Ha H K & S K Chough, 2003. Intermittent turbulent events over sandy current ripples: a motion-picture analysis of flume experiments. Sedimentary Geology, 161: 295-308

27 Kostaschuk R A & M A Church, 1993. Macroturbulence generated by dunes: Fraser River, Canada. Sedimentary Geology, 85: 25-37

28 Hennings I, D Herbers, K Prinz & F Ziemer, 2004. First results of the OROMA experiment in the Lister Tief of the German Bight in the North Sea. EARSeL eProceedings, 3: 86-104

29 Hennings I, B Lurin & N Didden, 2001. Radar imaging mechanism of the sea bed: Results of the C-STAR experiment in 1996 with special emphasis on the relaxation rate of short waves due to current variations. Journal of Physical Oceanography, 31: 1807-1827

30 Caponi E A, D R Crawford, H C Yuen & P G Saffman, 1988. Modulation of radar backscatter from the ocean by a variable surface current. Journal of Geophysical Research, 93(C6): 12249-12263